

Depth-resolved measurement of the compression displacement fields on the front and rear surfaces of an epoxy sample

WUCONG ZHANG¹, BO DONG¹, WEI ZHANG², ZHAOSHUI HE¹, SHENGLI XIE¹, YANZHOU ZHOU^{1*}

¹School of Automation, Guangdong University of Technology, Guangzhou, P.R. China, 510006

²Guangzhou Intellicash Equipment Co., Ltd., Guangzhou, P.R. China, 510663

*Corresponding author: zhouyanzhou@gdut.edu.cn

Compression is one of the typical parameters measured in material mechanics. In this research, the compression displacement fields on the front and rear surfaces of an epoxy sample are measured by using a tilt depth-resolved wavenumber-scanning Michelson interferometer. The light source is a distributed feedback laser diode, the wavenumber of which can be modulated to about $1.017 \times 10^4 \text{ m}^{-1}$ by the temperature without mode hopping. A random-sampling Fourier transform is designed to evaluate the phase differences before and after the applied loads. Experimental results show that the depth-resolved measurement of the compression displacement field is of high accuracy. It can be used to analyze force propagation inside resin-based composites.

Keywords: depth-resolved measurement, compression displacement field, wavenumber-scanning interferometry, epoxy.

1. Introduction

Subjecting an object to an applied load produces deformation or displacement in the whole body. Since the 1990s, phase-shifting interferometry (PSI) has been developed to measure the displacement perpendicular (out-of-plane) or parallel (in-plane) to the surface of an object [1]. In 2010, YANZHOU ZHOU *et al.* designed a 128-frame phase-shifting algorithm to measure the out-of-plane displacement at the bottom of a granular pack resulting from the indentation of the weight of 8-mm balls on BK7 glass [2]. The accuracy of this PSI was as high as $\pm 0.1 \text{ nm}$, and the method is robust. Recently, measurement of the displacement field inside the object using interferometry has begun [3–5].

The distribution of the in-plane displacement field can be mapped easily to mechanical parameters such as compression and tension. DE LA TORRE IBARRA *et al.* presented a phase-contrast spectral optical coherence tomography that can measure both in-plane and out-of-plane depth-resolved displacements within a sample consisting of a transparent water-based polymer rubber and two glass plates under applied shear loads [6].

By using three illuminations, CHAKRABORTY and RUIZ proposed using wavelength-scanning interferometry to measure the three-dimensional phase change at every voxel within the volume of a sample with a semitransparent scattering layer between two glass plates [7]. In this paper, depth-resolved wavenumber-scanning interferometry (DRWSI) is proposed to measure the in-plane compression displacement fields on the front and the rear surfaces of an epoxy sample by tuning the temperature of a distributed feedback laser diode. In the next two sections, we introduce the configuration of the optical system and depict the principle of tilt DRWSI. In the final two sections, we give out experimental results and present some conclusions.

2. Configuration of the experimental system

The experimental system was developed according to the principle of Michelson interferometry, as shown in Fig. 1. After the output of the laser is enlarged and aligned by a convex lens L , it is split into two beams by a 50:50 splitter cube. One beam illuminates the epoxy sample. Another illuminates a 6-mm-thick optical wedge with a tilt angle of $6'$. The optical wedge is used as reference surfaces and applied for wavelength monitoring at the same time. The reflected light from the sample and the optical wedge are combined by the cube again and form fringe patterns on the imaging plane of the CCD camera (CCD-1300QF, VDS Vosskuhler Co., with 1024×1024 pixels and 12-bit digital output). The polarizer P in the reference optical path is used to adjust the re-

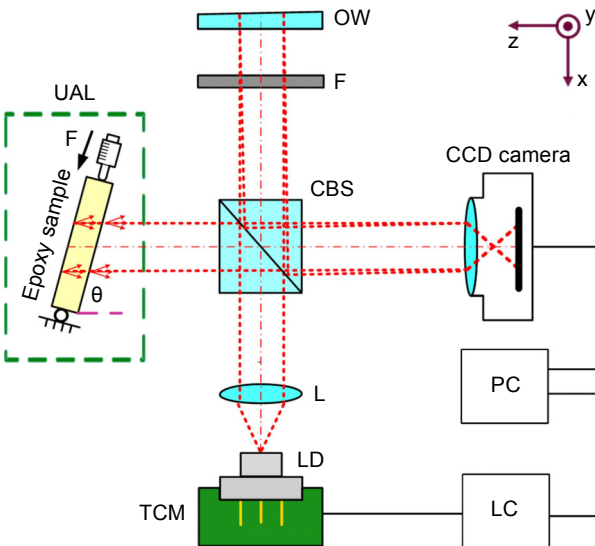


Fig. 1. Optical system configuration. UAL – applied load unit, θ – tilt angle, OW – optical wedge, F – filter, CBS – cube beam splitter, L – convex lens, LD – laser diode, TCM – temperature control unit, PC – personal computer, and LC – laser controller.

flected light intensity from the optical wedge to match the light from the sample to optimize the visibility of the fringe patterns.

The light source is a Toptica LD-0860-0150-DFB-1 laser diode, mounted on a TEC LD mount TCLDM9 (Thorlab Inc.) and driven by an ILX LDC 3724 laser diode controller (ILX Lightwave Co.). The laser wavelength, centered at 860 nm, can be tuned by 1.2 nm when its case temperature is changed from 40 to 20°C, while, over the same time, the CCD camera can collect 500 frames of wavenumber-resolved interference images. Therefore, the method used in this research is static. The range of wavenumber-scanning is $1.017 \times 10^4 \text{ m}^{-1}$. The depth resolution of the profile inside the sample is 0.618 mm, and the depth range is 77.2 mm. The root mean square error of measuring the displacement is $\pm 100 \text{ nm}$. The (x, y) resolution of the profile is $9.98 \text{ }\mu\text{m}/\text{pixel}$. The field of view is $10.12 \times 10.12 \text{ mm}$.

The epoxy sample is made by mixing an epoxy resin and curing agent in a volume ratio of 3:1 for 8 hours at room temperature. The epoxy sample size is $70 \times 55 \times 4.5 \text{ mm}$. It is polished by using 2000 grit sandpapers with a sand grain size of $0.74 \text{ }\mu\text{m}$ until its two surfaces are uniformly speckled.

As shown in Fig. 2, the epoxy sample is set up in the applied load unit, which is composed of two metal grooves and a metal base plate. On one side of the metal grooves, a round-head micrometer screw is installed. On the other side, two 5-mm-diameter steel balls are fixed onto the metal groove every 40 mm. The two small steel balls and the round-head micrometer screw form three-pivot point mechanical loading. The epoxy sample is slightly preloaded by finely adjusting the micrometer screw. A high-precision rotating platform is used to tilt the applied load unit at an angle $\theta = 80^\circ$ to the optical axis, as shown in Fig. 3. The load is applied to the epoxy sample as the micrometer screw is driven to generate a transverse displacement field.

Three groups of loading and displacement experiments were conducted with displacement of contact point (DCP) of 5, 10, and 20 μm , respectively. Wavenumber

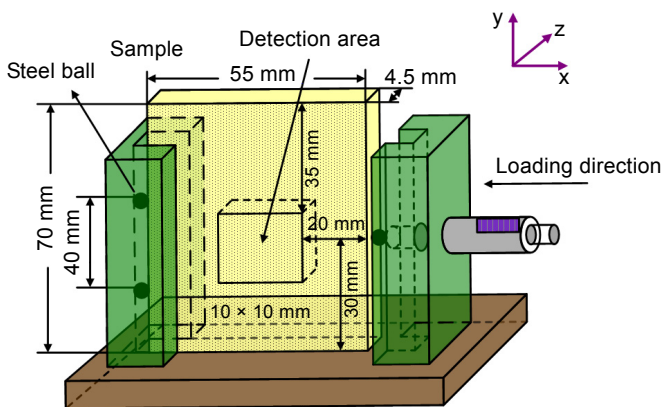


Fig. 2. Applied load unit.

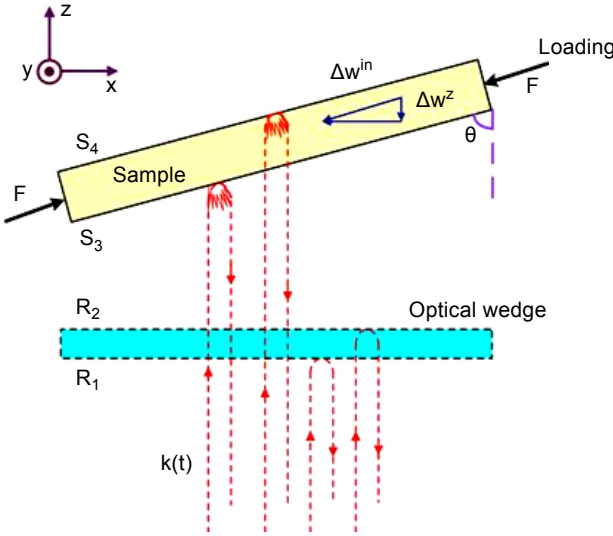


Fig. 3. Tilt Michelson interferometry.

-scanning interferometry is used to evaluate the compression displacement field on the front and rear surfaces of the epoxy sample, as described in the following.

3. Principle of tilt depth-resolved wavenumber-scanning interferometry

3.1. Measurement of the series of wavenumbers

To depict the interferometry clearly, we draw the optical paths and the reference plane together in Fig. 3. Its principle is shown in Figs. 1 and 3. R_1 , R_2 , S_3 , and S_4 represent the front and rear surfaces of the optical wedge and the epoxy sample, respectively, and θ is the tilt angle between the sample and the optical axis in the reference optical path. As the laser light is reflected from those surfaces, respectively, fringe patterns are formed on the imaging plane of the CCD camera. The series of fringe patterns photographed by the CCD camera can then be expressed as

$$I(x, y, k) = \sum_{p=1}^M \sum_{q=1}^M \sqrt{I_p(x, y)I_q(x, y)} \cos \left[2A_{pq}(x, y)k + \varphi_{pq0} \right] \quad (1)$$

$$A_{12}(x, y) = A_{120} + \Delta A_{12x}x + \Delta A_{12y}y \quad (2)$$

where the wavenumber $k = 2\pi/\lambda$ is tuned, as shown in Fig. 4a, as the temperature of the laser is modulated, (x, y) represents the spatial coordinates, M is the number of reflecting surfaces and M is 4 here, I is the reflective light intensity, the subscripts p and q represent the interference signal from positions p and q in depth, respectively, where 1 and 2 are the front and rear surfaces of the optical wedge, respectively, φ_{pq0} is

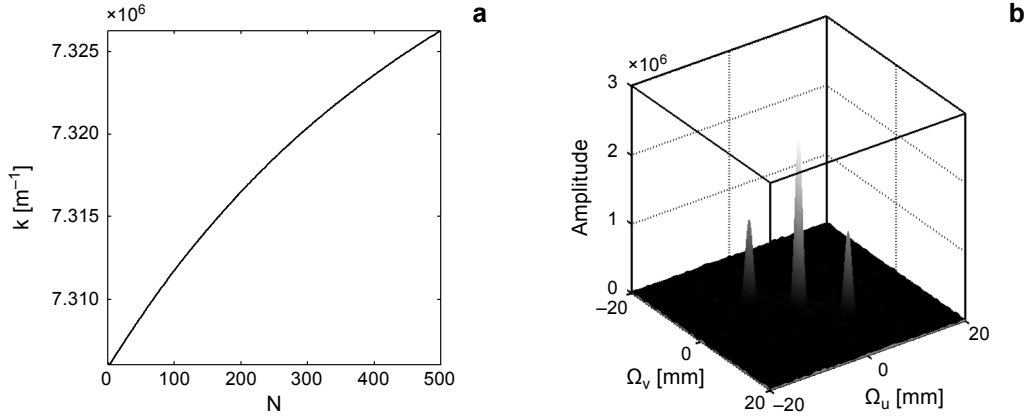


Fig. 4. Monitoring the wavenumber scanning series: wavenumber scanning series (a), and amplitude map of the interference from the optical wedge (b).

the initial interference phase between p and q , $A_{pq}(x, y)$ is the optical path length (OPL) between p and q , A_{120} is the OPL of the optical wedge in the original point, which is the upper left corner of the field of view photographed by the CCD camera, and ΔA_{12x} and ΔA_{12y} are the change of OPLs of the optical wedge per pixel along the x and y directions, respectively. The two-dimensional (2D) spatial Fourier transform of Eq. (1) is

$$F[I(u, v, k)] = \sum_{p=1}^M \sum_{q=1}^M \sqrt{I_p I_q} \delta[u \pm \Omega_{pqu}(k), v \pm \Omega_{pqv}(k)] \exp[\mu_j \Psi_{pq}(k)] \quad (3)$$

and

$$\begin{cases} \Omega_{12u}(k) = (\Delta A_{12x}/\pi)k \\ \Omega_{12v}(k) = (\Delta A_{12y}/\pi)k \\ \Psi_{12}(k) = 2A_{120}k + \varphi_{120} \end{cases} \quad (4)$$

and u, v are the 2D coordinates of the spatial frequency mapped from the x and y directions, respectively, $\delta(u, v)$ is the 2D delta function, Ω and Ψ are the spatial frequency and spatial phase, respectively; $\Omega_{12u}(k)$, $\Omega_{12v}(k)$, and $\Psi_{12}(k)$ are the spatial frequencies and spatial phase of the optical wedge as shown in Fig. 4b. Because the spatial phase of the optical wedge is linearly proportional to the wavenumber k , it can be expressed as

$$k = \frac{\Psi_{12}(k) - \varphi_{120}}{2A_{120}} \quad (5)$$

Equation (5) can be used to evaluate the wavenumber series of the light source in terms of the unwrapped spatial phase of the optical wedge; the result is shown in Fig. 4a.

3.2. Evaluation of the wrapped phase map

In order to eliminate the nonlinear effects of wavenumber scanning, the random-sampling Fourier transform (RSFT) is applied [8]. Using the RSFT, the fringe patterns $I(x, y, k)$ in k space can be written as

$$\tilde{I}(x, y, f) = \sum_{s=1}^S I[x, y, k(s)] w[k(s)] \exp[-j2\pi f k(s)] \quad (6)$$

where S is the total number of the images photographed by the CCD camera, $k(s)$ is the wavenumber as the CCD camera takes the s -th image, w is the window function, and f is the frequency in k space. Substituting Eq. (1) into Eq. (6), we obtain

$$\tilde{I}(x, y, f) = \sum_{p=1}^M \sum_{q=1}^M \sqrt{I_p(x, y) I_q(x, y)} \tilde{W}[f(x, y) \pm f_{pq}(x, y)] \exp[\pm j\varphi_{pq}(x, y)] \quad (7)$$

where

$$f_{pq}(x, y) = \frac{A_{pq}(x, y)}{\pi} \quad (8)$$

$$\varphi_{pq}(x, y) = 2A_{pq}(x, y)k_0 + \varphi_{pq0}(x, y) \quad (9)$$

where \tilde{W} is the frequency expression of the window function, $f_{pq}(x, y)$ and $\varphi_{pq}(x, y)$ are the peak frequency and phase from the interference signals p and q , respectively, and k_0 is the initial wavenumber of the light source.

The phase $\varphi_{pq}(x, y)$ in Eq. (9) is wrapped between $[-\pi, \pi)$, owing to the property of the tangent function; therefore, it is called the wrapped phase. After being unwrapped, it is linearly proportional to the OPL of the interference signal.

3.3. Evaluation of the distribution of the in-plane displacement on the front and rear surfaces of the epoxy sample

If the wrapped phases are $\varphi_{pq}^A(x, y)$ and $\varphi_{pq}^B(x, y)$ before and after loading, respectively, their difference is

$$\Delta\varphi_{pq}^{\text{wrp}}(x, y) = \tan^{-1} \left\{ \frac{\sin[\varphi_{pq}^B(x, y)] \cos[\varphi_{pq}^A(x, y)] - \cos[\varphi_{pq}^B(x, y)] \sin[\varphi_{pq}^A(x, y)]}{\cos[\varphi_{pq}^B(x, y)] \cos[\varphi_{pq}^A(x, y)] + \sin[\varphi_{pq}^B(x, y)] \sin[\varphi_{pq}^A(x, y)]} \right\} \quad (10)$$

The $\Delta\varphi_{pq}^{\text{wrp}}(x, y)$ is wrapped into $[-\pi, \pi)$ too; therefore, it needs to be unwrapped. The unwrapped or real phase difference before and after loading is

$$\Delta\varphi_{pq}^{\text{unwrp}}(x, y) = \text{unwrap}[\Delta\varphi_{pq}^{\text{wrp}}(x, y)] \quad (11)$$

The unwrapping process follows the method described in [9]. According to Eqs. (9) and (11), before and after loading, the displacement field inside the epoxy sample along the direction z is

$$\Delta w_{pq}^z(x, y) = \frac{\Delta \varphi_{pq}^{\text{unwrp}}(x, y)}{2k_0 n_{pq}} \quad (12)$$

where n_{pq} is the refractive index between signals p and q , which can be predetermined.

As shown in Fig. 3, the epoxy sample is set to a tilt angle θ with respect to the reference optical axis. The load is applied along the epoxy sample surface to produce only the compression displacement. The compression displacement field inside the epoxy sample is the in-plane displacement field, which can be deduced from the out-of-plane displacement field in the direction z , as shown in Fig. 3:

$$\Delta w_{pq}^{\text{in}}(x, y) = \frac{\Delta w_{pq}^z(x, y)}{\cos(\theta)} \quad (13)$$

4. Experimental results

A reflective white-light image of the epoxy sample is shown in Fig. 5a; the speckle on the front surface is clearly visible and the fringe pattern from the sample and the

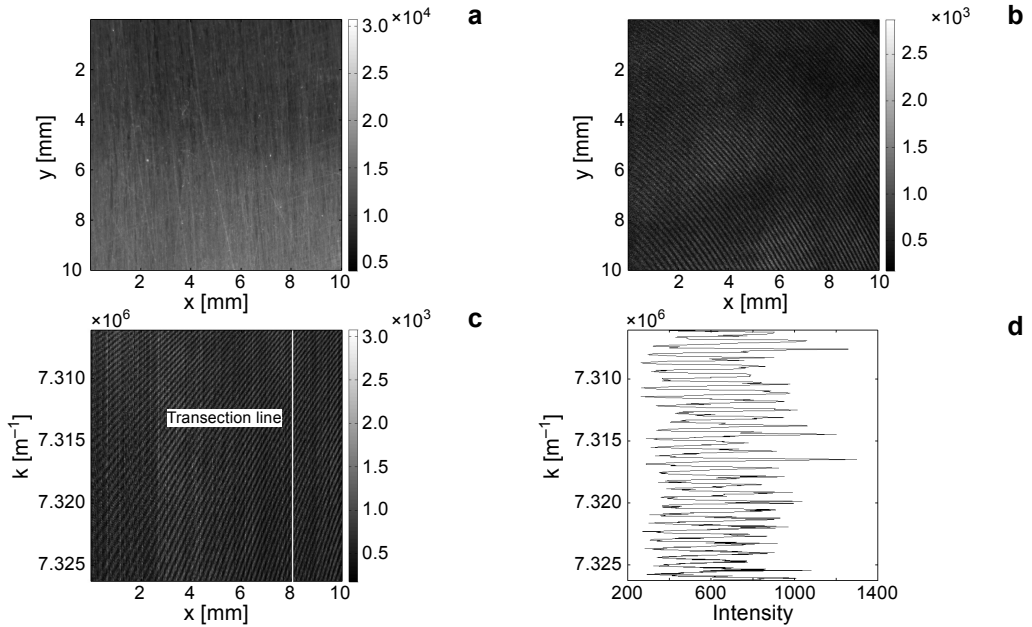


Fig. 5. Fringe pattern analysis of the epoxy sample. White-light image (a). Fringe pattern (b). The k -domain interference patterns at a line of $y = 5$ mm (c). The k -domain interference signal at a point $(x, y) = (8 \text{ mm}, 5 \text{ mm})$ (d).

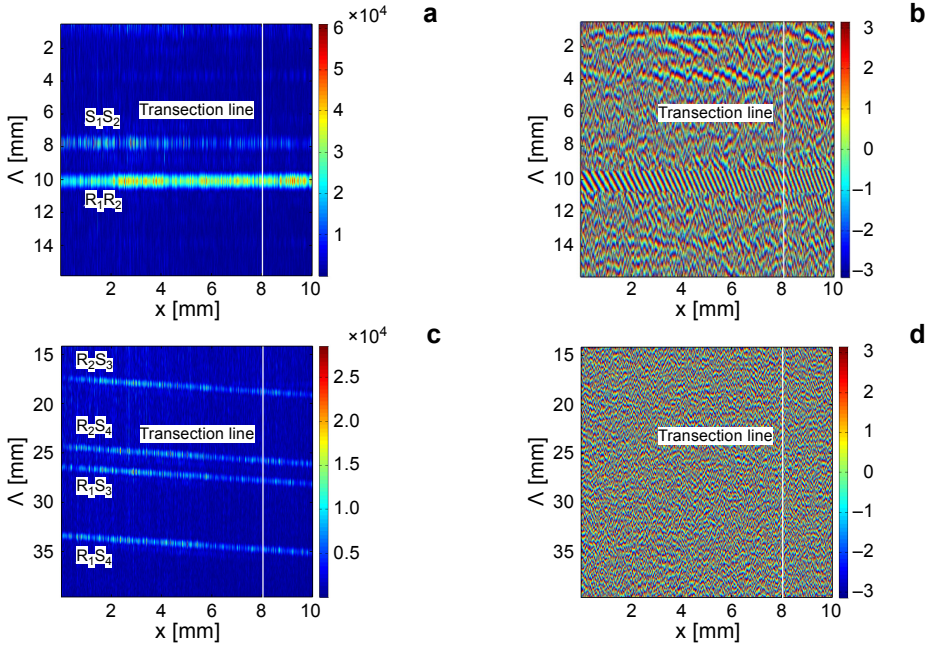


Fig. 6. Amplitude and phase maps of the interference patterns at the line $y = 5$ mm. The range of the OPL is from 0 to 15.8 mm (a, b), and from 14.2 to 39.6 mm (c, d).

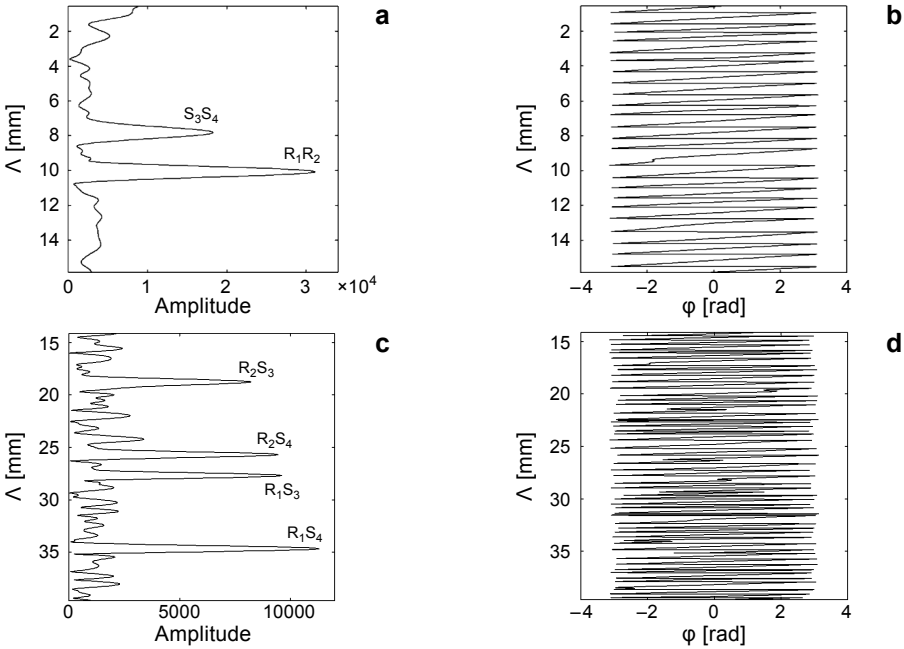


Fig. 7. Amplitude and phase maps of the interference signal at the point $(x, y) = (8 \text{ mm}, 5 \text{ mm})$. The range of the OPL is from 0 to 15.8 mm (a, b), and from 14.2 to 39.6 mm (c, d).

optical wedge is shown in Fig. 5b. The k -space interference signal at a line $y = 5$ mm in Fig. 5b is shown in Fig. 5c, and the k -space interference signal at $(x, y) = (8$ mm, 5 mm) in Fig. 5b is shown in Fig. 5d.

First, the relative wavenumber series as the fringe pattern is measured along the time axis. Each fringe pattern should be transformed to the 2D spatial frequency domain, according to Eq. (3), as shown in Fig. 4b. The phase at the peak of the optical wedge (see Fig. 4b) is extracted with respect to its fringe pattern to form a series of phases. After unwrapping, the wavenumber k is obtained, according to Eq. (5), as shown in Fig. 4a. After the wavenumber series is substituted into Eq. (6), the RSFT formula, the amplitude and phase maps of Fig. 5c can be created, as shown in Figs. 6a–6d, respectively. The amplitude and phase maps of Fig. 5d are shown in Figs. 7a–7d, respectively.

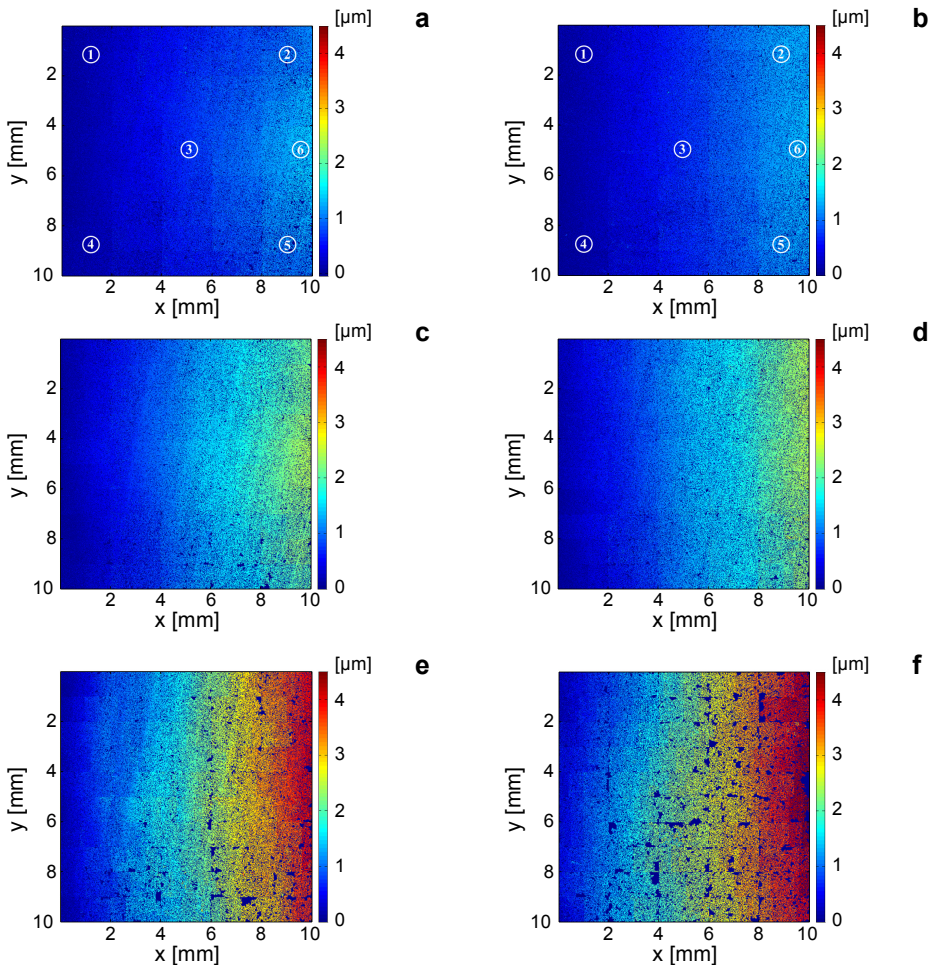


Fig. 8. Compression displacement fields on the front surface of the epoxy sample (a, c, e) and on the rear surface of the epoxy sample (b, d, f). The samples are subject to an applied DCP of 5 μm (a, b), of 10 μm (c, d), and of 20 μm (e, f).

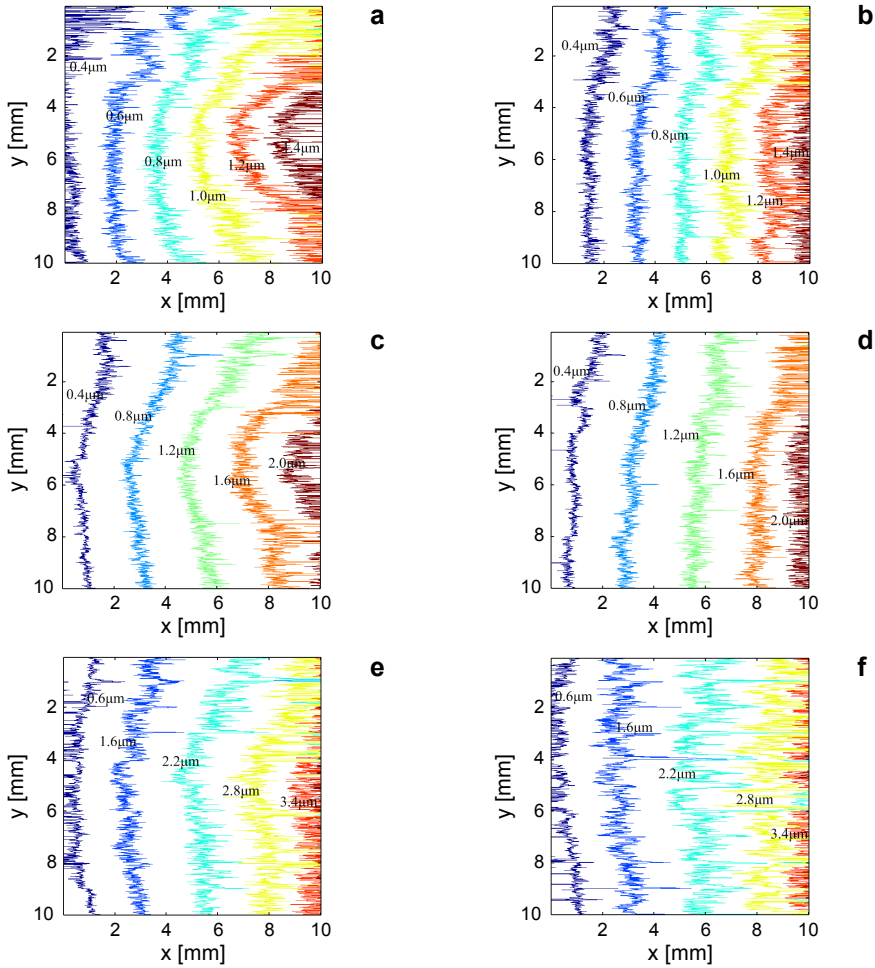


Fig. 9. Isoline contour plots of the compression displacements on the front surface (**a**, **c**, **e**) and on the rear surface (**b**, **d**, **f**) of the epoxy sample. The samples are subject to an applied DCP of $5\ \mu\text{m}$ (**a**, **b**), of $10\ \mu\text{m}$ (**c**, **d**), and of $20\ \mu\text{m}$ (**e**, **f**).

In Fig. 6c, the peaks in the amplitude, representing the interference signals between R_2S_3 , R_2S_4 , R_1S_3 , and R_1S_4 , respectively, are clearly obvious. In the same position of Fig. 7c, the interference signal between R_2S_3 , R_2S_4 , R_1S_3 , and R_1S_4 is also clearly visible, despite the speckle surfaces of the sample.

The phase at the amplitude peaks of R_2S_3 and R_2S_4 is extracted pixel by pixel in the whole field of view to form a map. Those phase values are located in the range $[-\pi, \pi)$, as discussed with respect to Eqs. (10)–(12). After phase unwrapping and in-plane displacement computation, the maps of the compression displacement field on the front (S_3) and rear (S_4) surfaces of the epoxy sample subjected to applied DCP of 5, 10, and $20\ \mu\text{m}$ can be calculated, as shown in Fig. 8. Their respective isoline contour plots are displayed in Fig. 9.

The compression displacement field is generally maximum to the left of the sample where the loading is applied and is the zero to the right of the sample where the two steel balls are located. Because the field of view is smaller than the displacement region of the sample as shown in Fig. 2, the maximum compression displacement in the field of view is smaller than the applied loads. Furthermore, the compression displacement

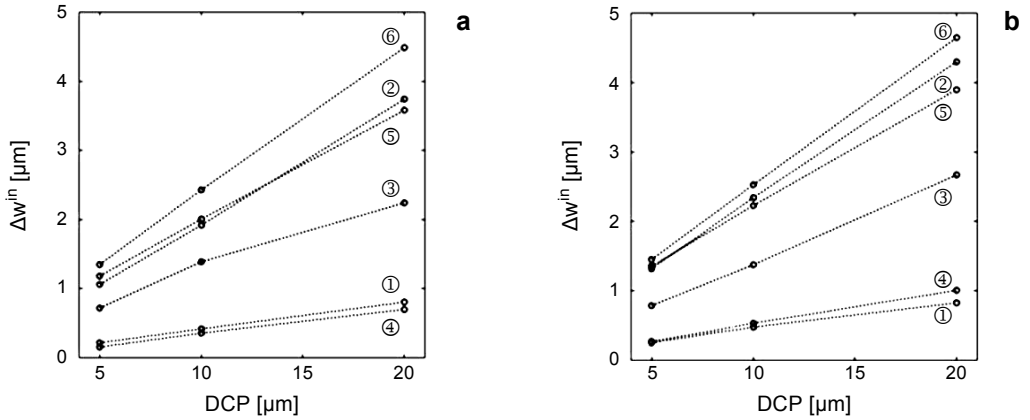


Fig. 10. Compression displacements vs. DCP at the points (1 mm, 1 mm), (1 mm, 9 mm), (5 mm, 5 mm), (9 mm, 1 mm), (9 mm, 9 mm), and (10 mm, 5 mm) on the front surface of the sample (a) and on the rear surface of the sample (b).

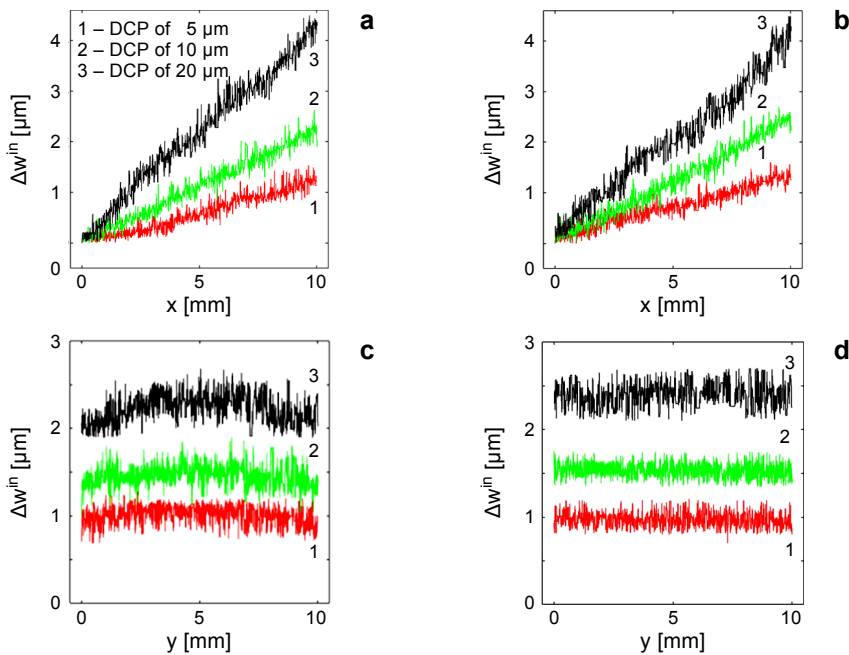


Fig. 11. Compression displacement vs. DCP at the lines $y = 5$ mm (a, b) and $x = 5$ mm (c, d). Front surface of the sample (a, c), and rear surface of the sample (b, d).

field decreases from the left to the right. Because at the left boundary of the field of view the initial phases are set to be zero, all the compression displacements are set to be zero at the left boundary; therefore, the measurement results are the relative compression displacement fields in the field of view. As seen in Fig. 9, the distribution and propagation of the displacement from the left to the right roughly follow along vertical line, because the loads are purely compressive and away from the field of view.

As shown in Figs. 8a and 8b, six points $(x, y) = (1 \text{ mm}, 1 \text{ mm}), (1 \text{ mm}, 9 \text{ mm}), (5 \text{ mm}, 5 \text{ mm}), (9 \text{ mm}, 1 \text{ mm}), (9 \text{ mm}, 9 \text{ mm}),$ and $(10 \text{ mm}, 5 \text{ mm})$ on the front and rear surfaces of the sample are chosen to evaluate the relation between the displacements and DCP, which is shown in Fig. 10. At the point $(x, y) = (10 \text{ mm}, 5 \text{ mm})$, the compression displacements on the front surface of the sample are 1.35, 2.43, and 4.49 μm , respectively, while they are 1.41, 2.54, and 4.67 μm on the rear surface of the sample, when the DCP are 5, 10, and 20 μm , respectively. The relation between the compression displacements and DCP at the lines $y = 5 \text{ mm}$ and $x = 5 \text{ mm}$ are shown in Fig. 11, respectively. It is concluded that the relationships between the compression displacement fields and DCP are approximately linear.

5. Conclusions

We have presented a way to measure the compression displacement field on the front and rear of speckled surfaces of a translucent epoxy sample by using tilt depth-resolved wavenumber-scanning interferometry. Since the sample is tilted about 80° to the optical axis, the use of this interferometry method makes it possible to measure the displacement in the z direction to ascertain the in-plane displacement. Using a device to apply only a compressive load, the compression displacement field on the front and rear surfaces of the epoxy sample are measured successfully. The proposed system and method have the following advantages:

1. It is a nondestructive, depth-resolved measurement that can be used to simultaneously measure the displacement fields of the internal reflective interfaces of the sample before and after loading.
2. The measurement of the compression displacement field is of high precision, with a root mean square error of $\pm 100 \text{ nm}$. The depth resolution of the profile measurement is 0.618 μm .
3. The signal-to-noise ratio is high and no numerical filtering is required in the data processing.
4. Without movable component, the measurement system is simple and reliable.

However, the proposed system does not take into account that a phase error will appear that may lead to spurious strains due to the non-constant magnification of the imaging lens, which can be improved by using a telecentric lens in further research. In summary, using tilt depth-resolved wavenumber-scanning interferometry to measure the compression displacement field in an epoxy sample has good application prospects.

Acknowledgements – The authors wish to thank Science and Technology Project of Guangdong Province (STPGP) (2016A020220017), and Guangzhou Science and Technology Program (201604016135).

References

- [1] RASTOGI P.K., *Digital Speckle Pattern Interferometry and Related Techniques*, 1st Ed., Wiley, 2001.
- [2] YANZHOU ZHOU, WILDMAN R.D., HUNTLEY J.M., *Measurement of the mechanical properties of granular packs by wavelength-scanning interferometry*, [Proceedings of the Royal Society of A: Mathematical, Physical and Engineering Sciences 466\(2115\)](#), 2010, pp. 789–808.
- [3] RUIZ P.D., YANZHOU ZHOU, HUNTLEY J.M., WILDMAN R.D., *Depth-resolved whole-field displacement measurement using wavelength scanning interferometry*, [Journal of Optics A: Pure and Applied Optics 6\(7\)](#), 2004, pp. 679–683.
- [4] RUIZ P.D., HUNTLEY J.M., WILDMAN R.D., *Depth-resolved whole-field displacement measurement by wavelength-scanning electronic speckle pattern interferometry*, [Applied Optics 44\(19\)](#), 2005, pp. 3945–3953.
- [5] YUN ZHANG, BO DONG, YULEI BAI, SHUANGLI YE, ZHENKUN LEI, YANZHOU ZHOU, *Measurement of depth-resolved thermal deformation distribution using phase-contrast spectral optical coherence tomography*, [Optics Express 23\(21\)](#), 2015, pp. 28067–28075.
- [6] DE LA TORRE IBARRA M.H., RUIZ P.D., HUNTLEY J.M., *Simultaneous measurement of in-plane and out-of-plane displacement fields in scattering media using phase-contrast spectral optical coherence tomography*, [Optics Letters 34\(6\)](#), 2009, pp. 806–808.
- [7] CHAKRABORTY S., RUIZ P.D., *Measurement of all orthogonal components of displacement in the volume of scattering materials using wavelength scanning interferometry*, [Journal of the Optical Society of America A 29\(9\)](#), 2012, pp. 1776–1785.
- [8] JINXIONG XU, YUFEI LIU, BO DONG, YULEI BAI, LINLIN HU, CONG SHI, ZHUOMING XU, YANZHOU ZHOU, *Improvement of the depth resolution in depth-resolved wavenumber-scanning interferometry using multiple uncorrelated wavenumber bands*, [Applied Optics 52\(20\)](#), 2013, pp. 4890–4897.
- [9] HUNTLEY J.M., *Noise-immune phase unwrapping algorithm*, [Applied Optics 28\(16\)](#), 1989, pp. 3268–3270.

*Received January 17, 2017
in revised form July 12, 2017*